A Novel Primary-Side Regulation Control Scheme for CCM and DCM *LLC* LED Driver Based on "Magnetizing Current Cancellation Method"

Hanjing Dong, Xiaogao Xie, *Member, IEEE*, Fengjiang Mao, Lina Zhang, and Yuanbin He, *Member, IEEE*

***Abstract*—In this article, the primary-side regulation (PSR) technique to achieve accurate output current in an *LLC* resonant converter has been studied. A novel PSR control scheme for an *LLC* light-emitting diode (LED) driver based on the "magnetizing current cancellation method" is proposed. The proposed "magnetizing current cancellation method" can effectively eliminate the effect of magnetizing current in the sampled primary resonant current under both the continuous conduction mode and the discontinuous conduction mode. Thus, the accurate output current can be estimated on the primary side of the *LLC* resonant converter. The magnetizing current cancellation method for the LLC LED driver with symmetric primary resonant current and asymmetric primary resonant current has been analyzed in detail. Some design considerations have also been presented. Then, an *LLC* PSR control circuit has been designed based on the theoretical analysis. Finally, a 48-to-78-V/1.3-A laboratory prototype for the LED driver has been built up, and experimental results show that good output current regulation has been obtained.**

***Index Terms*—*LLC*, output current estimation, primary-side regulation (PSR).**

NOMENCLATURE

CCM	Continuous conduction mode.
C_r	Resonant capacitor.
d_1, d_2	Duty cycles of v_{g_d1} and v_{g_d2}.
DCM	Discontinuous conduction mode.
f_r	Resonant frequency.
f_s	Switching frequency.
L_m	Magnetizing inductor of the transformer.
L_r	Resonant inductor.
I_o	Output current.
i_r	Resonant current.
i_{r_rec}	Rectified resonant current.
i_m	Magnetizing current.
I_m	Amplitude of magnetizing current in a symmetric *LLC* resonant converter.
I_{m1}	Positive amplitude of magnetizing current in an asymmetric *LLC* resonant converter.
$-I_{m2}$	Negative amplitude of magnetizing current in an asymmetric *LLC* resonant converter.
I_{mdc}	DC bias magnetizing current.
i_{m_rec}	Rectified magnetizing current.
I_{o_est}	Estimated output current.
i_s	Secondary current flowing through the secondary loop.
ΔI	Deviation between the estimated current I_{o_est} and the output current I_o.
$\Delta I'$	Deviation between the estimated output current and the output current if both the secondary leakage inductors are set to the large one.
N_p	Turns of primary winding of the transformer.
N_s	Turns of secondary winding of the transformer.
N_a	Turns of auxiliary winding of the transformer.
L_{ks1}, L_{ks2}	Secondary leakage inductors of the transformer.
S_1	Trapezoidal area formed by the virtual magnetizing current and period T_1.
S_2	Trapezoidal area formed by i_{m_rec} and period T_2.
S_3	Trapezoidal area formed by the virtual magnetizing current and period T_3.
S_4	Trapezoidal area formed by i_{m_rec} and period T_4.
S_{m1}	Triangle area formed by positive i_{m_rec} and the time axis in the first resonant period of the positive half cycle.
S_{m2}	Triangle area formed by negative i_{m_rec} and the time axis in the first resonant period of the positive half cycle.
S'_{m1}	Triangle area formed by positive i_{m_rec} and the time axis in the first resonant period of the negative half cycle.
S'_{m2}	Triangle area formed by negative i_{m_rec} and the time axis in the first resonant period of the negative half cycle.
$\overline{S}_1$–$\overline{S}_4$	Average value of S_1–S_4.
ΔS	Difference area between $S_{m1}+S_1$ and S_{m2}.
ΔS_1	Difference between the positive area and negative area formed by i_{m_rec} and the time axis in the positive half cycle.

Manuscript received September 6, 2019; revised December 9, 2019 and February 14, 2020; accepted April 13, 2020. Date of publication April 19, 2020; date of current version July 20, 2020. This work was supported in part by the Fundamental Research Funds for the Provincial Universities of Zhejiang under Grant GK199900299012-023 and in part by the National Natural Science Foundation of China under Grant 51707051. Recommended for publication by Associate Editor L. Huber. *(Corresponding author: Xiaogao Xie.)*

The authors are with the School of Automation, Hangzhou Dianzi University, Hangzhou 310018, China (e-mail: 174060001@hdu.edu.cn; xiexg@hdu.edu.cn; 181060022@hdu.edu.cn; zhanglina@hdu.edu.cn; yuanbinhe@hdu.edu.cn).

Color versions of one or more of the figures in this article are available online at https://ieeexplore.ieee.org.

Digital Object Identifier 10.1109/TPEL.2020.2989169

ΔS_2 Difference between the positive area and negative area formed by i_{m_rec} and the time axis in the negative half cycle.
$\overline{\Delta S_1}$,$\overline{\Delta S_2}$ Average values of ΔS_1 and ΔS_2.
T_r Resonant period.
T_s Switching period.
T_1 Period from the point that i_{r_rec} equals i_{m_rec} to the point that virtual magnetizing current reaches I_m or I_{m1} in the DCM.
T_2 Period of the second resonant region during positive half cycle in the DCM.
T_3 Period from the point that i_{r_rec} equals i_{m_rec} to the point that virtual magnetizing current reaches I_m or I_{m2} in the DCM.
T_4 Period of the second resonant region during negative half cycle in the DCM
T_{c1} First resonant region period during positive half cycle in the DCM.
T_{c2} First resonant region period during negative half cycle in the DCM.
v_{aux} Auxiliary winding voltage of the transformer.
v_{aux1} The part of $v_{\mathrm{aux\_rec}}$ located in the first resonant region.
v_{aux11} The part of $v_{\mathrm{aux\_rec}}$ located in the first resonant region of the positive half cycle.
v_{aux12} The part of $v_{\mathrm{aux\_rec}}$ located in the first resonant region of the negative half cycle.
v_{aux2} The part of $v_{\mathrm{aux\_rec}}$ located in the second resonant region in a symmetric *LLC* resonant converter.
v_{aux21} The part of $v_{\mathrm{aux\_rec}}$ located in the second resonant region of the positive half cycle.
v_{aux22} The part of $v_{\mathrm{aux\_rec}}$ located in the second resonant region of the negative half cycle.
$v_{\mathrm{aux\_rec}}$ Rectified voltage of auxiliary winding of the transformer.
V_{bias} Bias voltage reference.
v_{g1}, v_{g2} Driving signals of primary switches Q_1 and Q_2.
v_{g_d1}, v_{g_d2} Pulses represent the second resonant regions in positive and negative half cycles, respectively.
v_{im_com} Total magnetizing current compensation signal.
v_{Io_est} Estimated value of the output current.
v_{ir} Voltage signal of the sensed resonant current.
v_{ir_rav21} Positive half cycle magnetizing current compensation signal.
v_{ir_rav22} Negative half cycle magnetizing current compensation signal.
v_{ir_rec} Voltage signal representing rectified resonant current.
v_{ir_rec1} Voltage signal representing the rectified resonant current located in the first resonant region.
v_{ir1_avg} Average value of v_{ir_rec1}.
v_{ir_rec21} Voltage signal representing the rectified resonant current located in the second resonant region of the positive half cycle.
v_{ir21_avg} Average value of v_{ir_rec21}.
v_{ir_rec22} Voltage signal representing the rectified resonant current located in the second resonant region of the negative half cycle.
v_{ir22_avg} Average value of v_{ir_rec22}.
v_m Primary winding voltage.
v_n Pulse representing the negative half cycle.
v_{n1} Pulse obtained by comparing V_{bias} with v_{aux}.
V_o Output voltage.
v_p Pulse representing the positive half cycle.
v_{p1} Pulse obtained by comparing v_{aux} with $-V_{\mathrm{bias}}$.
v_{sm} Pulse representing the first resonant region of the resonant current.
$\overline{v}_{\mathrm{aux1}}$ Average amplitude of v_{aux1}.
$\overline{v}_{\mathrm{aux11}}$ Average amplitude of v_{aux11}.
$\overline{v}_{\mathrm{aux12}}$ Average amplitude of v_{aux12}.
$\overline{v}_{\mathrm{aux2}}$ Average amplitude of v_{aux2}.
$\overline{v}_{\mathrm{aux21}}$ Average amplitude of v_{aux21}.
$\overline{v}_{\mathrm{aux22}}$ Average amplitude of v_{aux22}.
$v_{\mathrm{aux21\_avg}}$ Average value of v_{aux21}.
$v_{\mathrm{aux22\_avg}}$ Average value of v_{aux22}.

I. Introduction

A LIGHT-EMITTING diode (LED) with its prominent characteristics, such as high brightness, small volume, high energy efficiency, and long lifetime, has gradually been used to replace the traditional lighting equipment in our daily life [1]. In contrast, as the brightness of an LED is determined by the dc input current, an innovative LED driver with high efficiency, high reliability, long lifetime, and low cost is also necessary. With the continuous breakthrough of LED technology, LED lighting is becoming the most promising source of light in the future. In recent years, it has been generally applied in urban lighting, LCD backlighting, street lighting, residential lighting, and medical treatment.

For ac–dc situations, the primary-side regulated (PSR) flyback topology, which has the advantages of simple structure, electrical isolation, and low cost, has drawn more and more attention in low-power applications such as LED drivers and chargers [2]–[9]. To reduce the cost, the flyback converter usually regulates the output current and serves as the power factor corrector (PFC) simultaneously, which is known as the single-stage PFC technique. However, for higher power levels, the single-stage flyback converter cannot satisfy the efficiency demand due to poor transformer utilization.

Thus, the two-stage ac–dc structure with a PFC front stage is the preferred choice for high-power applications, although the cost and size both increases. For the front PFC stage, the boost converter is a good candidate topology and has been applied popularly. For the end stage, the flyback converter and the *LLC* resonant converter are the most popular candidate topologies. However, the transmission power with a cascaded boost PFC and a flyback converter is usually limited to be lower than 80 W. The half-bridge *LLC* (HB-*LLC*) resonant topology, which always operates in the resonant mode with pulse frequency modulation, can realize zero-voltage switching for the primary switches and

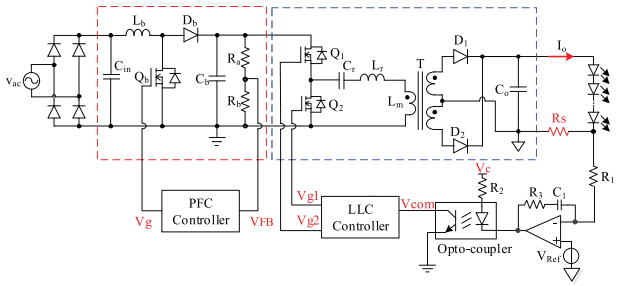

Fig. 1. Two-stage ac–dc LED driver based on a cascaded boost PFC and an HB-*LLC* resonant converter.

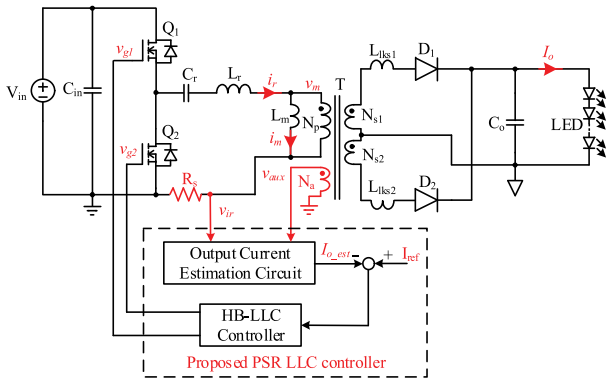

Fig. 2. Schematic of the HB-*LLC* converter with the proposed PSR controller.

achieves high efficiency and high power density. Thus, it has been widely applied in high-power LED driver equipment as the end stage [10]–[20].

In the conventional *LLC* resonant LED driver, the output current is sensed on the secondary side and sent to the regulated circuit. Then, the generated regulated signal is sent to the primary side with an optocoupler, as shown in Fig. 1. The secondary circuit and the optocoupler have increased the overall cost of the converter. Moreover, the optocoupler also reduces the lifetime of the converter [2].

The output current PSR technique can resolve the mentioned problem by removing the secondary regulation circuit and the optocoupler. PSR techniques for the flyback converter are well developed [2]–[9], and there are a number of commercial integrated chips for the PSR flyback converter.

However, there are few studies focusing on the output current PSR technique for the *LLC* resonant converter till now. The reason is that the magnetizing current of the transformer has been included in the primary resonant current, and it is difficult to extract the output current information from the primary resonant current directly.

The magnetizing current and the resonant current can be separated by adding an external parallel-resonant inductor, as shown in [10]. The inductance of the external inductor is much lower than the magnetizing inductance of the transformer. The resonant current is much larger than the magnetizing current in the transformer, and the magnetizing current of the transformer can be nearly neglected. Therefore, the current in the primary winding can reflect the load current directly. However, the external inductor increases the cost and the size of the converter greatly. In [10], an improved circuit was further proposed to reduce the volume of the added inductor. As shown in [10, Fig. 10], an external compensating inductor is inserted between the auxiliary winding and the current-sensing resistor, and an antiphase emulated magnetizing current is generated and flows into the current-sensing resistor. In this way, the influence of the magnetizing current can be eliminated. However, the inductance tolerance makes a great influence on the output current regulation. Similar concept has been applied to the current-driven synchronous rectifier technique for the *LLC* resonant converter. In order to cancel out the magnetizing current's effect, the current transformer with compensating winding was proposed in [11].

In this article, the PSR technique for achieving accurate output current regulation in the *LLC* resonant converter has been studied. A novel *LLC* PSR control scheme based on the "magnetizing current cancellation method" is proposed, as shown in Fig. 2. The proposed *LLC* PSR controller consists of an output current estimation circuit and a conventional HB-*LLC* controller. The proposed output current estimation circuit is used to generate the estimated output current signal only with detected primary-side current and auxiliary winding voltage. A conventional HB-*LLC* controller receives the estimated output current value as a feedback signal to regulate the output current.

The proposed PSR controller can achieve an accurate output current under the CCM and the DCM by effectively eliminating the effect of the magnetizing current from the sampled primary resonant current. The magnetizing current cancellation method for the *LLC* LED driver with symmetric primary currents and asymmetric primary currents has been analyzed in Sections II and III, respectively. Section IV gives some design considerations, and specific realization of the control circuit based on the proposed method is presented in Section V. Experimental results based on a laboratory-made prototype are provided in Section VI. Finally, Section VII concludes this article.

II. Output Current Estimation for the *LLC* Resonant Converter With Symmetric Primary Current Waveforms

Usually, a well-designed *LLC* resonant converter has symmetric primary current waveform. The principle of output current estimation on the primary side under this condition will be analyzed in this section.

As we know, the *LLC* resonant converter operates in the CCM as the switching frequency f_s is higher than the resonant frequency f_r, while it operates in the DCM on the contrary.

A. Analysis on the LLC *Resonant Converter With Symmetric Primary Current Waveforms When Operating in the CCM*

When the *LLC* resonant converter operates in the CCM, the main waveforms are shown in Fig. 3. Obviously, the difference between the rectified resonant current i_{r_rec} and the rectified magnetizing current i_{m_rec} is the current transferred to the secondary side. Based on above analysis, the output current I_o

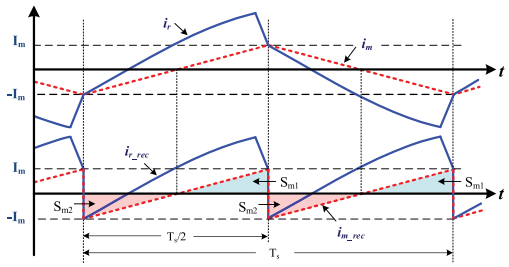

Fig. 3. Key waveforms of the symmetric *LLC* resonant converter operating in the CCM.

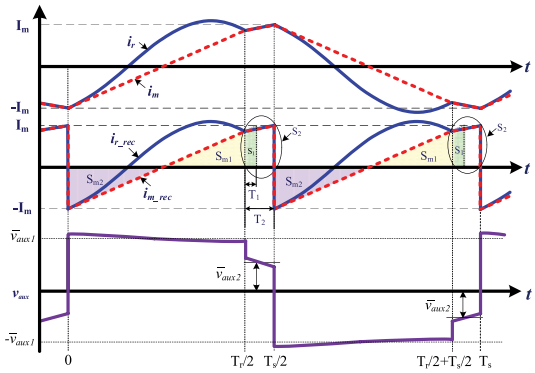

Fig. 4. Key waveforms of the symmetric *LLC* resonant converter operating in the DCM.

can be expressed as

$$I_o = \frac{2N_p}{N_s T_s} \int_0^{T_s/2} [i_{r\_rec}(t) - i_{m\_rec}(t)]\, dt \tag{1}$$

where i_{r_rec} can be obtained from the sampled resonant current i_r. However, the magnetizing current i_m cannot be sampled directly, so does i_{m_rec}. Therefore, the PSR controller cannot be designed according to (1) directly.

To solve this problem, a "magnetizing current cancellation method" is proposed. As shown in Fig. 3, the triangle area S_{m1} is equal to S_{m2} because of the symmetrical characteristic of i_{m_rec}, which means that the periodic average value of i_{m_rec} is zero. Therefore, (1) can be rewritten as

$$I_o = \frac{2N_p}{N_s T_s} \int_0^{T_s/2} i_{r\_rec}(t) dt. \tag{2}$$

Equation (2) means that the information of the output current can be obtained only by sampling i_r.

B. Analysis on the LLC *Resonant Converter With Symmetric Primary Current Waveforms and Operating in the DCM*

When the *LLC* resonant converter operates in the DCM, the main waveforms are shown in Fig. 4. A half switching cycle can be divided into two intervals: $[0,\ T_r/2]$ and $[T_r/2,\ T_s/2]$.

Stage 1 $[0,\ Tr/2]$*:* During this interval, the resonant capacitor C_r resonates with the resonant inductor L_r and the voltage v_m is clamped by the output voltage. This region is defined as the "first resonant region."

Stage 2 $[Tr/2,\ Ts/2]$*:* During this interval, C_r resonates with L_r and L_m, while the output diodes are both OFF. At the same time, L_m resonates with the parasitic capacitor across the primary winding of the transformer, which produces an oscillated voltage waveform across the primary winding. This region is defined as the "second resonant region."

The output current in the DCM can be described as

$$I_o = \frac{2N_p}{N_s T_s} \int_0^{T_r/2} [i_{r\_rec}(t) - i_{m\_rec}(t)]\, dt. \tag{3}$$

Similar to the CCM, the same idea of "magnetizing current cancellation method" is also applied to the DCM. However, the areas of the two parts S_{m1} and S_{m2}, as shown in Fig. 4, are not equal in the DCM because there exists the second resonant region in a half switching cycle. Therefore, the "magnetizing current cancellation method" cannot be applied directly. In order to eliminate the influence of i_m, an improved "magnetizing current cancellation method" is developed.

As we know, i_m has different slopes during intervals $[0,\ T_r/2]$ and $[T_r/2,\ T_s/2]$. Herein, we suppose there is a virtual magnetizing current, which will continue to increase after time $T_r/2$ with the same slope during the interval $[0,\ T_r/2]$. The virtual magnetizing current forms a trapezoidal area S_1 with period T_1. According to geometric theory, it can be deduced that

$$S_{m2} = S_{m1} + S_1. \tag{4}$$

Therefore, the magnetizing current can be eliminated from the resonant current if S_1 can be obtained.

The periodic average value $\bar{S}_1$ of area S_1 can be expressed as

$$\bar{S}_1 = \frac{[i_{r\_rec}(T_r/2) + I_m]\, T_1}{2T_s}. \tag{5}$$

Obviously, it is difficult to obtain $\bar{S}_1$ directly because T_1 is difficult to obtain. Herein, an indirect way to obtain $\bar{S}_1$ is described as follows.

As shown in Fig. 4, the periodic average value of area S_2 can be expressed as

$$\bar{S}_2 = \frac{[i_{r\_rec}(T_r/2) + I_m] T_2}{2T_s}. \tag{6}$$

According to (5) and (6), the relationship between $\bar{S}_1$ and $\bar{S}_2$ is derived as

$$\frac{\bar{S}_1}{\bar{S}_2} = \frac{T_1}{T_2}. \tag{7}$$

In addition, because the increment value of the virtual magnetizing current during T_1 is equal to the increment value of the magnetizing current during T_2, a new equation can be derived as

$$I_m - i_{i\_rec}(T_r/2) = \frac{N_p \overline{v}_{\text{aux1}}}{N_a L_m} T_1 = \frac{N_p \overline{v}_{\text{aux2}}}{N_a L_m} T_2. \tag{8}$$

According to (7) and (8), it can be derived that

$$\bar{S}_1 = \bar{S}_2 \frac{\overline{v}_{\text{aux2}}}{\overline{v}_{\text{aux1}}}. \tag{9}$$

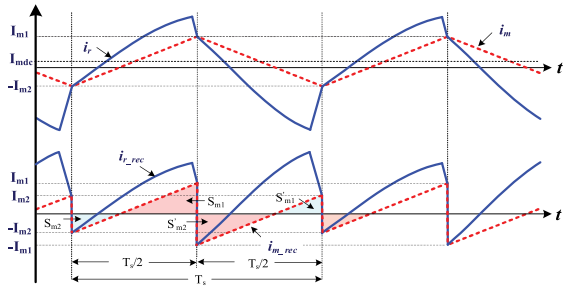

Fig. 5. Key waveforms of the asymmetric HB-*LLC* resonant converter operating in the CCM.

Substituting (4) and (9) into (3), the output current in the DCM can be expressed as

$$I_o = \frac{2N_p}{N_s}\left(\frac{1}{T_s}\int_0^{T_r/2} i_{r\_rec}(t)dt + \bar{S}_2\frac{\overline{v}_{aux2}}{\overline{v}_{aux1}}\right). \quad (10)$$

$\overline{v}_{aux1}$ and $\overline{v}_{aux2}$ can be obtained from the auxiliary winding of the transformer, and $\bar{S}_2$ can be obtained with the sampled primary resonant current during period T_2. Therefore, the information of I_o can be obtained on the primary side of the transformer, which means that primary regulation on the output current is feasible for the *LLC* resonant converter with symmetric discontinuous primary currents by using the proposed "magnetizing current cancellation method."

III. Output Current Estimation for the *LLC* Resonant Converter With Asymmetric Primary Current Waveforms

For the practical *LLC* resonant converter, the primary resonant currents will be asymmetric when some parameters of the converters are not ideal. There are two main reasons that will cause this problem: one is asymmetric pulse signals for primary switches Q_1 and Q_2, and the other is unequal values of transformer secondary leakage inductors L_{lks1} and L_{lks2} [21].

There exist three possible asymmetric cases: 1) continuous resonant current; 2) discontinuous resonant current; and 3) continuous resonant current in a half switching cycle and discontinuous resonant current in another half switching cycle. Output current estimation methods for these three cases will be discussed independently.

A. Analysis on the LLC Resonant Converter With Asymmetric Primary Current Waveforms When Operating in the CCM

Fig. 5 shows the key waveforms of the *LLC* resonant converter operating in the CCM with asymmetric primary current waveforms. The positive and negative amplitudes of the magnetizing current i_m are also asymmetric, which makes i_{m_rec} have different initial values in two neighboring half switching cycles. In a switching cycle, i_{m_rec} and the time axis form four triangle areas, named as S_{m1}, S_{m2}, S'_{m1}, and S'_{m2}, respectively. Obviously, the areas of S_{m1} and S_{m2} are different, which means that the magnetizing current cannot be eliminated in a half switching cycle. However, it can be deduced according to the geometric theory that the areas of S_{m1} and S'_{m2} are identical, while the

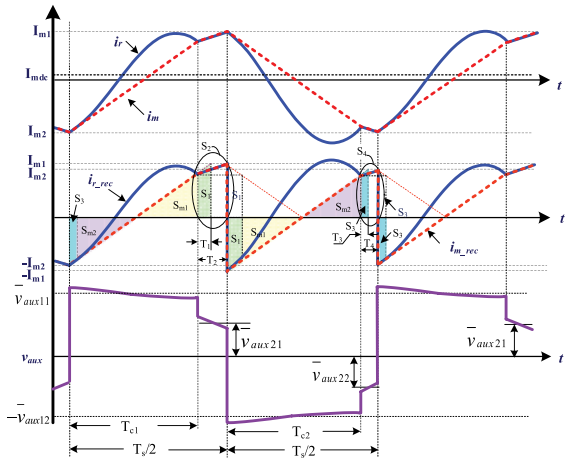

Fig. 6. Key waveforms of the asymmetric HB-*LLC* resonant converter operating in the DCM.

areas of S_{m2} and S'_{m1} are identical, i.e.,

$$\int_0^{T_s} i_{m\_rec}(t)dt = -S'_{m2} + S_{m1} - S_{m2} + S'_{m1} = 0. \quad (11)$$

Equation (11) means that the rectified magnetizing current can be eliminated in a switching cycle. Similarly, the output current can be derived as

$$\begin{aligned} I_o &= \frac{N_p}{N_s T_s}\int_0^{T_s}\left[i_{r\_rec}(t) - i_{m\_rec}(t)\right]dt \\ &= \frac{N_p}{N_s T_s}\int_0^{T_s} i_{r\_rec}(t)dt. \end{aligned} \quad (12)$$

Equation (12) means that the information of the output current of the *LLC* resonant converter operating in the CCM with asymmetric primary current waveforms can also be obtained on the primary side only by sampling i_r.

B. Analysis on the LLC Resonant Converter With Asymmetric Primary Current Waveforms When Operating in the DCM

Fig. 6 shows the key waveforms of the *LLC* resonant converter operating in the DCM with the asymmetric primary current waveforms. The half cycle is defined as the "positive half cycle" when v_{aux} is positive, while the other half cycle is defined as the "negative half cycle" when v_{aux} is negative.

According to geometric theory, the triangle area formed by the negative part of i_{m_rec} and the time axis in the positive half cycle is equal to $S_3 + S_{m2}$, while the triangle area formed by the negative part of i_{m_rec} and the time axis in the negative half cycle is equal to $S_1 + S_{m1}$. Because S_{m2} and S_{m1} can offset each other, the periodic average value of i_{m_rec} can be obtained as

$$\frac{1}{T_s}\left[\int_0^{T_{c1}} i_{m\_rec}(t)dt + \int_{T_s/2}^{T_s/2+T_{c2}} i_{m\_rec}(t)dt\right] = -(\bar{S}_1 + \bar{S}_3) \quad (13)$$

where

$$\bar{S_1} = \frac{[i_{r\_rec}(T_{c1}) + I_{m1}]T_1}{2T_s} \tag{14}$$

$$\bar{S_3} = \frac{[i_{r\_rec}(T_s/2 + T_{c2}) + I_{m2}]T_3}{2T_s}. \tag{15}$$

Similar to the condition of the *LLC* resonant converter with symmetric waveforms in the DCM, it can be derived that

$$\bar{S_1} = \bar{S_2}\frac{\overline{v}_{\text{aux21}}}{\overline{v}_{\text{aux11}}} = \frac{[i_{r\_rec}(T_{c1}) + I_{m1}]T_2}{2T_s} \cdot \frac{\overline{v}_{\text{aux21}}}{\overline{v}_{\text{aux11}}} \tag{16}$$

$$\bar{S_3} = \bar{S_4}\frac{\overline{v}_{\text{aux22}}}{\overline{v}_{\text{aux12}}} = \frac{[i_{r\_rec}(T_s/2 + T_{c2}) + I_{m2}]T_4}{2T_s} \cdot \frac{\overline{v}_{\text{aux22}}}{\overline{v}_{\text{aux12}}}. \tag{17}$$

Thus, the output current under this condition can be expressed as

$$\begin{aligned} I_o &= \frac{N_p}{N_s T_s}\left\{\int_0^{T_{c1}} [i_{r\_rec}(t) - i_{m\_rec}(t)]\,dt \right. \\ &\quad \left. + \int_{T_s/2}^{T_s/2+T_{c2}} [i_{r\_rec}(t) - i_{m\_rec}(t)]\,dt\right\} \\ &= \frac{N_p}{N_s}\left[\frac{1}{T_s}\left[\int_0^{T_{c1}} i_{r\_rec}(t)dt + \int_{T_s/2}^{T_s/2+T_{c2}} i_{r\_rec}(t)dt\right]\right. \\ &\quad \left. + \bar{S_2}\frac{\overline{v}_{\text{aux21}}}{\overline{v}_{\text{aux11}}} + \bar{S_4}\frac{\overline{v}_{\text{aux22}}}{\overline{v}_{\text{aux12}}}\right]. \end{aligned} \tag{18}$$

$\overline{v}_{\text{aux11}} - \overline{v}_{\text{aux22}}$ can be obtained from the auxiliary winding of the transformer, while $\bar{S}_2$ and $\bar{S}_4$can be obtained with the sampled primary resonant current and detected second resonant periods. Therefore, primary regulation on the output current is feasible for the *LLC* converter with asymmetric discontinuous primary currents by using the proposed "magnetizing current cancellation method."

C. Analysis on the LLC Resonant Converter With Asymmetric Primary Current Waveforms When Operating in the CCM and the DCM

When the *LLC* resonant converter operates around the resonant frequency while the parameters are asymmetric, it will come into a condition that the one half cycle waveforms are continuous and the other half cycle waveforms are discontinuous, as shown in Fig. 7.

In a switching cycle, i_{m_rec} and the time axis form four triangle areas named as S_{m1}, S_{m2}, S'_{m1}, and S'_{m2}, respectively. According to geometric theory, the area of S_{m2} is equal to the area of S'_{m1}.

Similarly, it can be deduced that

$$S'_{m2} = S_{m1} + S_1. \tag{19}$$

The average value $\bar{S}_1$ can be obtained with (16). Thus, the output current under this condition can be expressed as

$$\begin{aligned} I_o &= \frac{N_p}{N_s T_s}\left\{\int_0^{T_{c1}} [i_{r\_rec}(t) - i_{m\_rec}(t)]\,dt \right. \\ &\quad \left. + \int_{T_s/2}^{T_s} [i_{r\_rec}(t) - i_{m\_rec}(t)]\,dt\right\} \end{aligned}$$

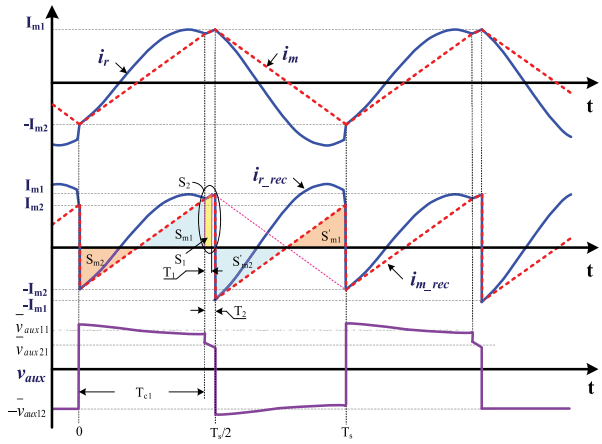

Fig. 7. Key waveforms of the asymmetric HB-*LLC* resonant converter operating in the CCM and the DCM.

$$= \frac{N_p}{N_s}\left[\frac{1}{T_s}\left[\int_0^{T_{c1}} i_{r\_rec}(t)dt + \int_{T_s/2}^{T_s} i_{r\_rec}(t)dt\right] + \bar{S_2}\frac{\overline{v}_{\text{aux21}}}{\overline{v}_{\text{aux11}}}\right]. \tag{20}$$

IV. Design Consideration

A. Effect of Transformer Leakage Inductors on Estimation Deviation of the Output Current

If the secondary leakage inductors of the transformer are equal ($L_{lks1} = L_{lks2} = L_{\text{lks}}$), the transformer primary winding voltage v_m during the output diodes conduction periods can be derived as

$$v_m(t) = \begin{cases} \frac{N_p}{N_s}\left[V_o + L_{\text{lks}}\frac{di_s(t)}{dt}\right], & 0 < t \le T_{c1} \\ -\frac{N_p}{N_s} & \\ \left[V_o + L_{\text{lks}}\frac{di_s(t-T_s/2)}{dt}\right], & T_s/2 < t \le T_s/2 + T_{c2}. \end{cases} \tag{21}$$

The slope of magnetizing current i_m can be obtained as

$$\frac{di_m(t)}{dt} = \begin{cases} \frac{N_p}{N_s}\left[\frac{V_o}{L_m} + \frac{L_{\text{lks}}}{L_m}\frac{di_s(t)}{dt}\right], & 0 < t \le T_{c1} \\ -\frac{N_p}{N_s} & \\ \left[\frac{V_o}{L_m} + \frac{L_{\text{lks}}}{L_m}\frac{di_s(t-T_s/2)}{dt}\right], & T_s/2 < t \le T_s/2 + T_{c2}. \end{cases} \tag{22}$$

Equation (22) indicates that the slope of i_m is not linear when leakage inductors of the transformer are taken into consideration. As an example, suppose that the currents of the HB-*LLC* resonant converter are symmetrical when operating in the DCM; the waveforms of the rectified primary current considering the effects of leakage inductors are shown in Fig. 8.

Obviously, the negative area S_{m2} cannot be offset by the positive area S_{m1} plus the compensation area S_1 under this condition.

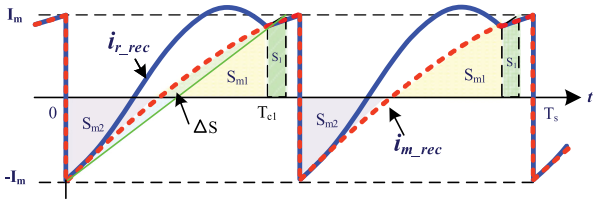

Fig. 8. Symmetrical waveforms of i_{r_rec} and i_{m_rec} in the DCM when leakage inductors are taken into account.

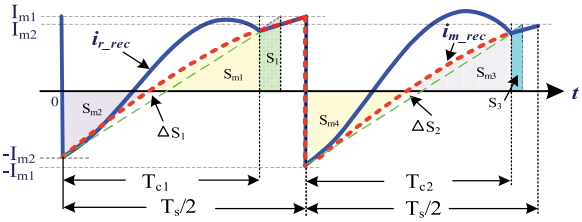

Fig. 9. Asymmetrical waveforms of i_{r_rec} and i_{m_rec} in the DCM when leakage inductors are taken into account.

According to (22), the expression of i_{m_rec} during the period $[0,\ T_{c1}]$ can be obtained as

$$i_{m\_\mathrm{rec}}(t) = -I_{\mathrm{m}} + \frac{N_p}{N_s}\frac{V_o}{L_m}\cdot t + \frac{N_p}{N_s}\frac{L_{\mathrm{lks}}}{L_m}\cdot i_s(t),\ 0 < t \le T_{c1}\,. \tag{23}$$

According to (23) and the waveforms shown in Fig. 8, it is easy to know that the difference area between $S_{m1}+S_1$ and S_{m2} is

$$\Delta S = S_{m1} + S_1 - S_{m2} = \frac{N_p}{N_s}\frac{L_{\mathrm{lks}}}{L_m}\cdot\int_0^{T_{c1}} i_s(t)dt. \tag{24}$$

ΔS will cause a deviation ΔI between the output current estimated by (10) and the real output current, i.e.,

$$\Delta I = \overline{\Delta S} = \frac{N_p}{N_s}\frac{L_{\mathrm{lks}}}{L_m} I_o. \tag{25}$$

Equation (25) indicates that ΔI is constant if the parameters of the converter are determined while the converter keeps operating in the DCM, which means that good output current regulation can be achieved. Moreover, this deviation can be offset by adjusting the current reference to obtain the desired output current.

However, when the HB-*LLC* resonant converter operates in the CCM with symmetrical current waveforms, $\overline{\Delta S}$ will decrease as the frequency increases, which causes the output current regulation error. The maximal possible output current regulation error can be evaluated with (25) if the HB-*LLC* converter operates in the CCM and DCM hybrid mode. For example, if the secondary leakage inductors reflected to the primary side are 1% of the magnetizing inductor and the turns ratio of the transformer is 3, the calculated maximal output current deviation is about 0.33%. Obviously, smaller ratio of leakage inductors to magnetizing inductor can help reduce the output current regulation deviation.

As an example, suppose that the currents of the HB-*LLC* resonant converter are asymmetrical when operating in the DCM; the rectified primary current waveforms considering the effects of leakage inductors are shown in Fig. 9.

According to the waveforms shown in Fig. 9, the difference between the positive area and negative area formed by $i_{m\_\mathrm{rec}}(t)$ and the time axis in the positive switching cycle is

$$\Delta S_1 = S_{m1} + S_1 - S_{m2} = \frac{N_p}{N_s}\frac{L_{\mathrm{lks1}}}{L_m}\cdot\int_0^{T_{c1}} i_s(t)dt. \tag{26}$$

Similarly, the difference between the positive area and the negative area formed by $i_{m\_\mathrm{rec}}(t)$ and the time axis in the negative half switching cycle is

$$\Delta S_2 = S_{m3} + S_3 - S_{m4} = \frac{N_p}{N_s}\frac{L_{\mathrm{lks2}}}{L_m}\cdot\int_{T_s/2}^{T_s/2+T_{c2}} i_s(t)dt. \tag{27}$$

Hence, it can be derived that

$$\overline{\Delta S_1} + \overline{\Delta S_2} = \frac{1}{T_s L_m}\frac{N_p}{N_s} \times \left[L_{\mathrm{lks1}}\int_0^{Tc1} i_s(t)dt + L_{\mathrm{lks2}}\int_{Ts/2}^{Ts/2+Tc2} i_s(t)dt\right]. \tag{28}$$

ΔS_1 and ΔS_2 represent the areas introduced by the nonlinear part in $i_{m\_\mathrm{rec}}(t)$, which cause the deviation between the estimated output current and the real output current.

According to (28), to calculate the estimation deviation, the expression of $i_s(t)$ should be obtained first. However, it is difficult to derive the accurate expression of $i_s(t)$ under this condition. However, the error ΔI can be evaluated in a simple way as follows.

Suppose that L_{lks2} is larger than L_{lks1}; the estimation error $\Delta I'$ caused by the symmetric leakage inductor L_{lks2} can be derived as

$$\Delta I' = \frac{N_p}{N_s}\frac{L_{\mathrm{lks2}}}{L_m} I_o. \tag{29}$$

$\Delta I'$ can be used to evaluate the real estimation error. Though $\Delta I'$ is a little bigger than the real value, the complex asymmetrical condition does not need to consider any more.

B. Effect of Asymmetrical Primary Switches Driving Pulses on Estimation Deviation of the Output Current

The asymmetrical primary driving signals also cause asymmetrical primary resonant current and magnetizing current. Suppose the secondary leakage inductors are equal; it is not difficult to derive that the deviation ΔI can also be expressed as (25). For simplicity, this condition is not analyzed in detail.

C. Effect of Transformer Leakage Inductors on the Voltage Across the Magnetizing Inductor

When the HB-*LLC* resonant converter has asymmetric secondary leakage inductors and operates in the DCM, it can be

derived that

$$v_m(t) = \begin{cases} \frac{N_p}{N_s}\left[V_o + L_{\text{lks1}}\frac{di_s(t)}{dt}\right], & 0 < t \le T_{c1} \\ -\frac{N_p}{N_s}\left[V_o + L_{\text{lks2}}\frac{di_s(t-T_s/2)}{dt}\right], & T_s/2 < t \le T_s/2 + T_{c2} \end{cases} \tag{30}$$

$$\int_0^{T_{c1}} \frac{di_s(t)}{dt}dt = 0, \quad \int_{T_s/2}^{T_s/2+T_{c2}} \frac{di_s(t-T_s/2)}{dt}dt = 0. \tag{31}$$

Substituting (31) into (30) and considering the voltage relationship between primary and auxiliary windings, it can be derived that

$$\overline{v}_{\text{aux11}} = \overline{v}_{\text{aux12}}. \tag{32}$$

Equation (32) means that the average amplitudes of the auxiliary winding voltage during the first resonant period in different half switching cycles are not affected by the leakage inductors in the DCM. Therefore, the unified equation of the estimated output current for the hybrid CCM and DCM HB-*LLC* converter can be expressed in eq. (33) shown at the bottom of this page

V. Realization of the Proposed PSR Controller

Based on (33), shown at the bottom of this page, the proposed PSR controller for the *LLC* resonant converter is designed, as shown in Fig. 10. Some key waveforms inside the controller are shown in Fig. 11. Detailed circuit implementation of the proposed controller is depicted in the following.

A. Detection of "Positive Half Cycle" and "Negative Half Cycle"

As mentioned in Section II, the rectified resonant current i_{r_rec} obtained from i_r according to the polarity of the transformer winding voltage is used for output current estimation.

As shown in Fig. 10, a simple detection circuit that consists of two comparators is used to detect the polarity of v_{aux}. As mentioned, there exists oscillation in the second resonant region, and higher *Q* factor of resonant parameters usually causes more severe oscillation. If the oscillation amplitude of v_{aux} falls below zero level during the positive half cycle or arises over zero level during the negative half cycle, the detection results will be incorrect. To prevent producing fault detection results, the comparison references of the comparators are biased. Besides, a cross-lock circuit formed with switches S_p and S_n is added and placed after the outputs of the comparators.

Fig. 12 shows the simulation results with SIMetrix/SIMPLIS software. It shows that proper detection results can be achieved even under severe oscillation condition.

B. Achieving the Rectified Resonant Current $\mathrm{i}_{\mathrm{r}\,\cdot rec}$ and the Rectified Auxiliary Winding Voltage $\mathrm{v}_{aux\,\cdot rec}$

When half cycle signals v_p and v_n are obtained, the active rectifiers with four switches, a hold-up capacitor, and a differential amplifier, as shown in Fig. 13(a), are used to achieve the rectified resonant current i_{r_rec} and rectified auxiliary winding voltage $v_{\text{aux\_rec}}$. Fig. 13(b) shows the signal transmission path during the positive half switching cycle when switches S_{x1} and S_{x4} are turned ON. The input signal forwardly transmits to capacitor C_x. Fig. 13(c) shows the signal transmission path during the negative half switching cycle when the switches S_{x2} and S_{x3} are turned ON. The input signal transmits to C_x reversely. The differential amplifier circuit is used to transform the floating voltage signal across C_x to a ground-referred signal.

There are two advantages of achieving the rectified waveform $v_{\text{aux\_rec}}$ with an active rectifier rather than an diode-based rectifier. First, only one pin is needed to get the input signal and the other pin is the ground pin of the controller. Second, the voltage drop across the active switches is much smaller, which is important for sampling the accurate auxiliary winding voltage in the following function circuits.

C. Detecting Resonant Current Regions

A knee point detector is used to detect the first resonant region, as shown in Fig. 10. The knee point detector is realized with a phase-shift circuit and logic units similar to the circuit shown in [22]. Corresponding waveforms during the operation process are shown in Fig. 11, where $v_{\text{aux\_rcd}}$ is achieved from $v_{\text{aux\_rec}}$ by the phase-shift circuit composed of R_{3a}, R_{3b}, and C_2. A reset signal v_{dms} is then generated by comparing $v_{\text{aux\_rcd}}$ with $v_{\text{aux\_rec}}$, while signals v_p and v_n are served as set signal of reset-set (RS) flip-flops U_{rs1} and U_{rs2}, respectively. Thereafter, the region signals v_{sm}, v_{g_d1} and v_{g_d2} are generated after some logical processes.

D. Extracting the First Resonant Current

The first resonant current is extracted by the first resonant current extraction circuit shown in Fig. 10. The signal v_{ir_rec1} is the part of the rectified resonant current in the first resonant region, which is obtained from the rectified resonant current signal v_{ir_rec} by a switch network with the control signal v_{sm}.

$$I_o = \frac{N_p}{N_s} \cdot \left\{ \underbrace{\frac{1}{T_s}\left[\int_0^{T_{c1}} i_{r\_\text{rec}}(t)dt + \int_{T_s/2}^{T_s/2+T_{c2}} i_{r\_\text{rec}}(t)dt\right]}_{\text{First resonant region current}} + \underbrace{\bar{S}_2\frac{\overline{v}_{\text{aux21}}}{\overline{v}_{\text{aux1}}} + \bar{S}_4\frac{\overline{v}_{\text{aux22}}}{\overline{v}_{\text{aux1}}}}_{\text{magnetizing current compensation}} \right\} \tag{33}$$

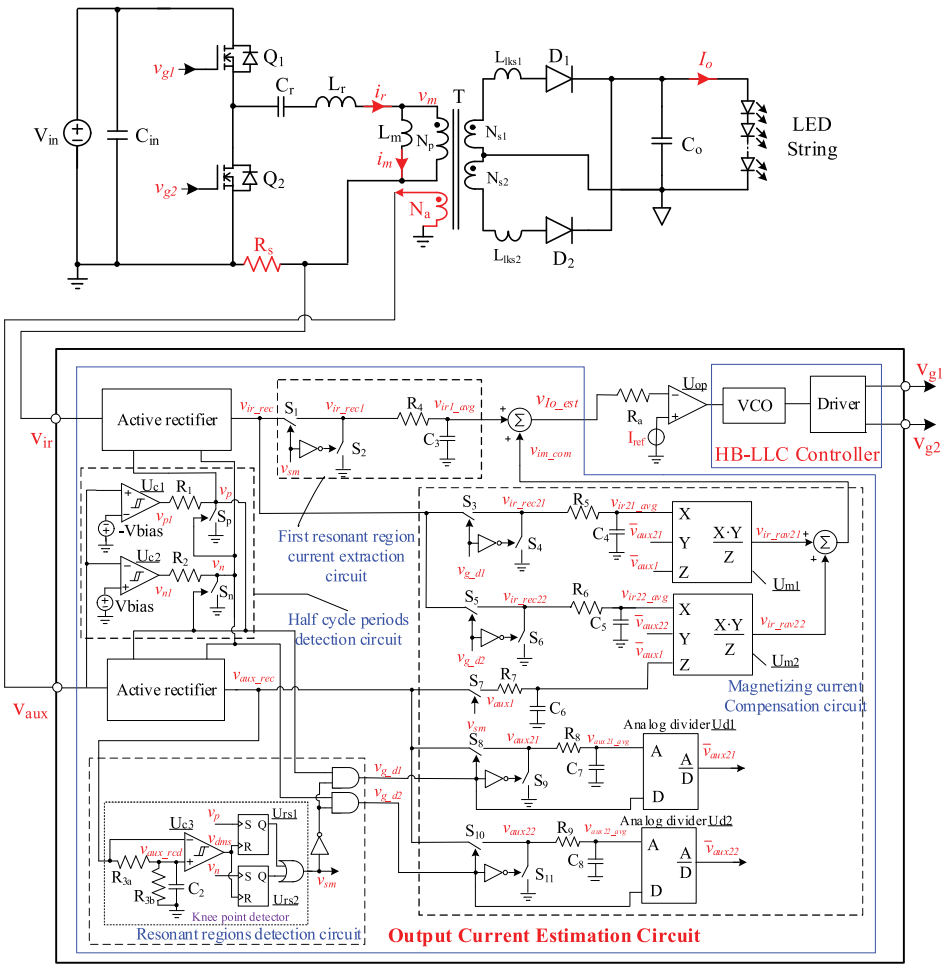

Fig. 10. Schematic of the *LLC* resonant converter with the proposed output current estimation circuit.

The average value of v_{ir_rec1} is obtained as follows:

$$v_{ir1\_avg} = \frac{1}{T_s}\int_0^{T_s} v_{ir\_rec1}(t)dt = \frac{1}{T_s} \times \left[\int_0^{T_{c1}/2} v_{ir\_rec}(t)dt + \int_{T_s/2}^{T_s/2+T_{c2}/2} v_{ir\_rec}(t)\right] dt. \quad (34)$$

E. Magnetizing Current Compensation

Magnetizing current compensation is the key issue of the proposed control, the implementation circuit of which can be realized according to (33), and the procedure is as follows.

As shown in Fig. 10, $\bar{v}_{\rm aux1}$ is achieved from $v_{\rm aux\_rec}$ by using a switch average network formed by S_7, R_7, and C_6. Switch S_7 is controlled by the generated first resonant current region signal v_{sm}.

Because there exists oscillation on the waveform of $v_{\rm aux}$ in the DCM, the process to achieve $\bar{v}_{\rm aux21}$ and $\bar{v}_{\rm aux22}$ is little complex. First, the waveforms v_{aux21} and v_{aux22} are extracted from $v_{\rm aux}$ with switching networks are formed by switches S_8, S_9 and S_{10}, S_{11}, respectively. Then, the average values of v_{aux21} and v_{aux22}, i.e., v_{aux21_avg} and v_{aux22_avg}, are obtained with *RC* filters. Finally, v_{aux21_avg}, v_{g_d1} and v_{aux22_avg}, v_{g_d2} are sent to the analog dividers U_{d1} and U_{d2} separately.

Thus, $\bar{v}_{\rm aux21}$ and $\bar{v}_{\rm aux22}$ can be obtained according to the function of the analog divider [23], as follows:

$$\bar{v}_{\rm aux21} = \frac{v_{\rm aux21\_avg}}{d_1}, \quad \bar{v}_{\rm aux22} = \frac{v_{\rm aux22\_avg}}{d_2}. \quad (35)$$

where d_1 is the duty cycle of v_{g_d1} and d_2 is the duty cycle of v_{g_d2}.

The rectified resonant current signals v_{ir_rec21} and v_{ir_rec22} in the second resonant region can also be extracted from v_{ir_rec} by switching networks with resonant current region signals v_{g_d1} and v_{g_d2}. The average values of v_{ir_rec21} and v_{ir_rec22} in a switching period can be further obtained with *RC* filters and are expressed as follows:

$$v_{ir21\_avg} = \frac{1}{T_s}\int_0^{T_s} v_{ir\_rec21}dt = \overline{S_2} \quad (36)$$

$$v_{ir22\_avg} = \frac{1}{T_s}\int_0^{T_s} v_{ir\_rec22}dt = \overline{S_4}. \quad (37)$$

Then, the signals v_{ir21_avg}, $\bar{v}_{\rm aux21}$, and $\bar{v}_{\rm aux1}$ are sent into the multiplier U_{m1}, while the signals v_{ir22_avg}, $\bar{v}_{\rm aux22}$, and $\bar{v}_{\rm aux1}$ are sent into the multiplier U_{m2}. Then, the compensation values

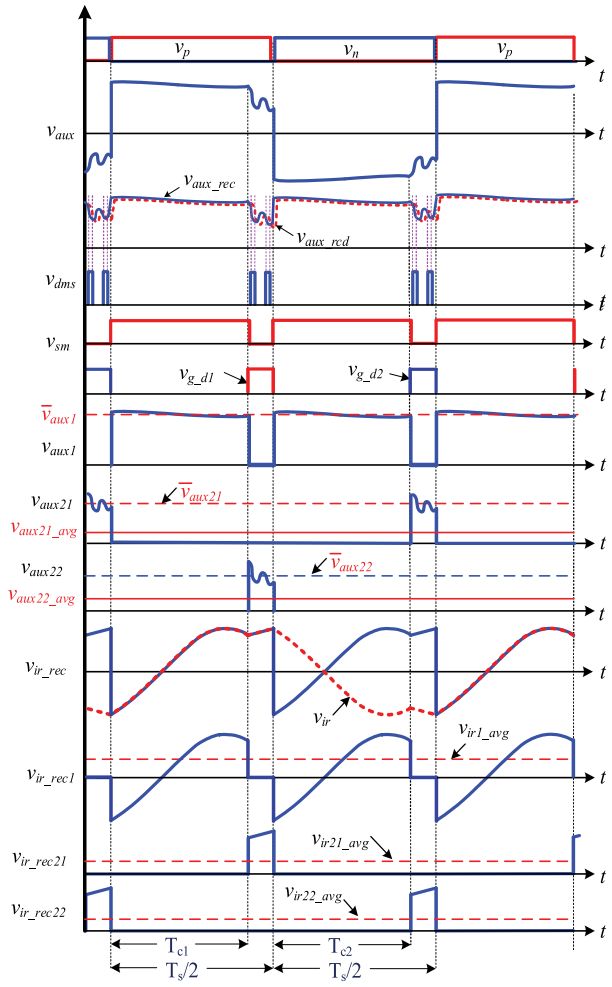

Fig. 11. Main waveforms inside the proposed PSR controller.

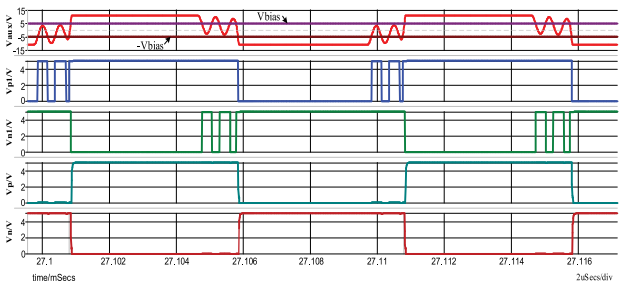

Fig. 12. Simulation waveforms of the half cycle detection circuit.

v_{ir_rav21} and v_{ir_rav22} can be obtained, as follows:

$$v_{ir\_rav21} = \frac{v_{ir21\_avg} \cdot \overline{v}_{aux21}}{\overline{v}_{aux1}} = \overline{S}_2 \frac{\overline{v}_{aux21}}{\overline{v}_{aux1}} \quad (38)$$

$$v_{ir\_rav22} = \frac{v_{ir22\_avg} \cdot \overline{v}_{aux22}}{\overline{v}_{aux1}} = \overline{S}_4 \frac{\overline{v}_{aux22}}{\overline{v}_{aux1}}. \quad (39)$$

A summing circuit is used to sum up the values of v_{ir_rav21} and v_{ir_rav22} so that the magnetizing current compensation signal v_{im_com} is achieved. Furthermore, by summing the average value of the first resonant current v_{ir1_avg} and the compensation

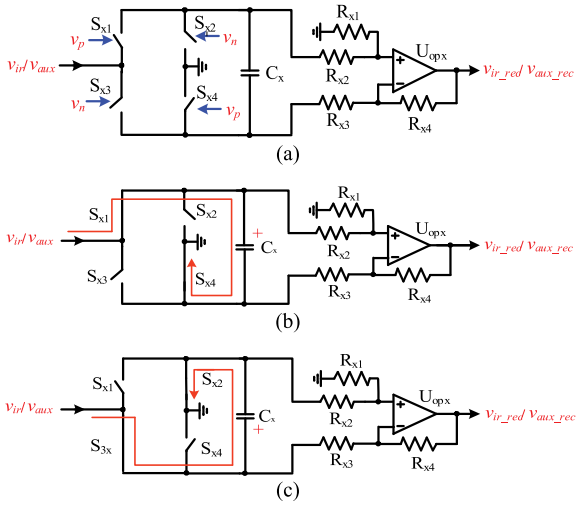

Fig. 13. Active rectifier to obtain v_{ir_rec} and v_{aux_rec}. (a) Implementation circuit. (b) Signal transmission path during the positive half switching cycle. (c) Signal transmission path during the negative half switching cycle.

signal v_{im_com}, the estimated output current signal v_{Io_est} is achieved. When the *LLC* resonant converter operates in the CCM, the magnetizing current does not need to be compensated, and the compensation signal v_{im_com} equals zero.

There are several low-pass filters formed by the resistor and the capacitor in the proposed PSR control circuit for achieving average values of signals. The cutoff frequency of *RC* filters should be low enough to filter the switching ripple. These *RC* filters do not generate signal transmission delay but may slow down the closed-loop regulation if their parameters are not appropriately designed. To avoid this, the cutoff frequency of *RC* filters should be larger than the closed-loop bandwidth. The parameter selection of *RC* filters follows the aforementioned principles.

The estimated output current signal v_{Io_est} is sent to an amplifier to generate an amplified error signal. The pulse generator based on a voltage-controlled oscillator (VCO) is identical to the popular commercial *LLC* control ICs, which is not introduced in detail in this article.

VI. Experimental Results

To verify the theoretical analysis, a laboratory prototype of a 48-to-78-V/1.3-A HB-*LLC* LED driver with the designed PSR controller has been built up, as shown in Fig. 14. The parameters of the prototype components are listed in Table I. The control circuit is realized with discrete components and the conventional *LLC* controller L6599 from ST Ltd. Considering a variation range of the output voltage, the resonant frequency is set to be 65 kHz at $V_o = 60$ V under a nominal input voltage of 400 V. Under the nominal input voltage, the prototype is designed to operate in the CCM when the output voltage is lower than 60 V, while it works in the DCM with larger output voltage.

The key waveforms of the proposed control circuit with the symmetric primary current ($L_{lks1} = L_{lks2} = 1.3\,\mu$H) are shown in Figs. 15–18. Fig. 15 describes the operation process of achieving v_{ir_rec} with the active rectifier. With the obtained pulse

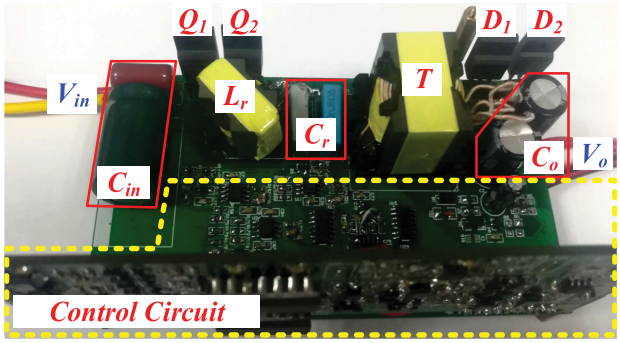

Fig. 14. Photo of the experimental prototype.

TABLE I
PARAMETERS OF THE LABORATORY PROTOTYPE COMPONENTS

Component	Parameters
Input voltage V_{in}	380~420 V, V_{in_nom}=400V
Output voltage V_o	48V~78V
Main switches Q_1, Q_2	ISA07N65A, 7A/650V
Resonant inductor L_r	240μH
Resonant capacitor C_r	25nF
Transformer T	Core:PQ2625, L_m=1.5mH, N_p: N_{s1}: N_{s2}: N_a =40:12:12:3
Output Diode D_1, D_2	SBD10C200F, 10A/200V
Output Capacitor C_o	2×220μF/100V

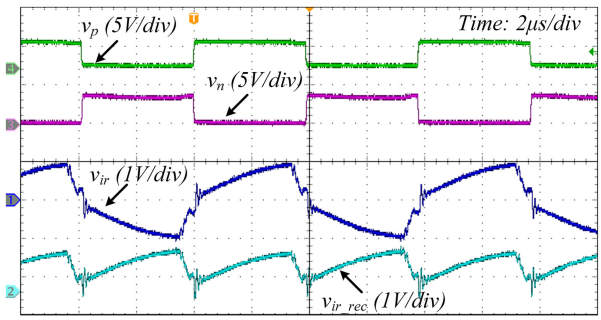

(a)

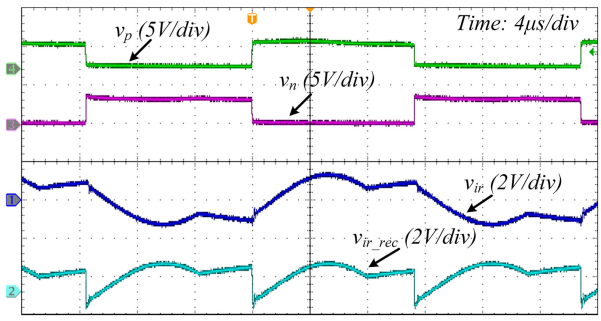

(b)

Fig. 15. Measured waveforms of pulse signals v_p, v_n and sampling signals v_{ir}, v_{r_rec} in the symmetric condition ($V_{\rm in}$ = 400 V). (a) CCM (V_o = 51 V and I_o = 1.3 A). (b) DCM (V_o = 75 V and I_o = 1.3 A).

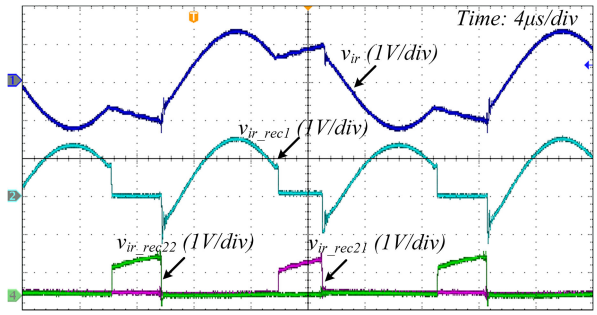

Fig. 16. Measured waveforms of v_{ir}, v_{ir_rec1}, v_{ir_rec21}, and v_{ir_rec22} in the DCM ($V_{\rm in}$ = 400 V, V_o = 75 V, and I_o = 1.3 A).

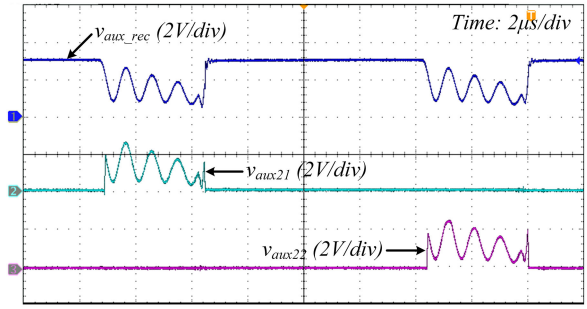

(a)

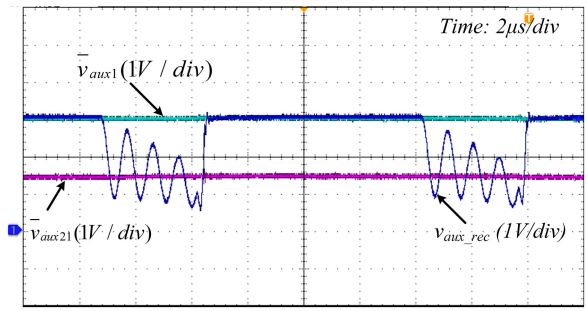

(b)

Fig. 17. Operation process of auxiliary winding voltage sampling in the DCM ($V_{\rm in}$ = 400 V, V_o = 75 V, and I_o = 1.3 A). (a) Measured waveforms of $v_{\rm aux\_rec}$, $v_{\rm aux\_21}$, and $v_{\rm aux\_22}$. (b) Measured waveforms of $v_{\rm aux\_rec}$, $\bar{v}_{\rm aux1}$ and $\bar{v}_{\rm aux21}$.

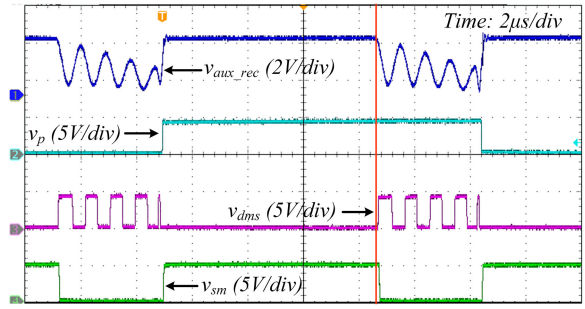

Fig. 18. Key waveforms of the knee point detector in the DCM.

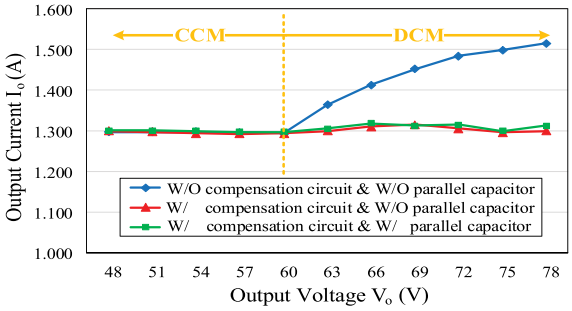

Fig. 19. Measured curves of the output current under different conditions ($V_{\rm in}$ = 400 V, with symmetrical circuit parameters).

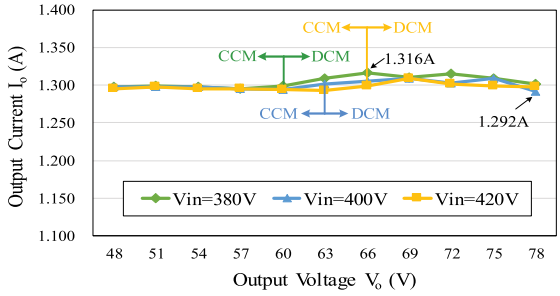

Fig. 20. Measured curves of the output current versus output voltage under different input voltages (with symmetric circuit parameters).

signals v_p and v_n, v_{ir_rec} can be generated from the sampled resonant current signal v_{ir}.

Fig. 16 presents the measured waveforms of v_{ir}, v_{ir_rec1}, v_{ir_rec21}, and v_{ir_rec22} in the DCM. It can be seen that the waveform of v_{ir_rec} has been divided into three parts successfully.

The auxiliary winding voltage waveforms in the DCM are shown in Fig. 17. Fig. 17(a) shows the waveforms of the rectified auxiliary winding voltage $v_{\rm aux\_rec}$ and extracted waveforms $v_{\rm aux\_21}$ and $v_{\rm aux\_22}$. Obvious oscillation on the waveform of $v_{\rm aux\_rec}$ during the second resonant region can be observed, which is caused by the resonance between the magnetizing inductor L_m and parasitic capacitors. The measured average waveforms $\bar{v}_{\rm aux21}$ and $\bar{v}_{\rm aux1}$ are shown in Fig. 17(b). $\bar{v}_{\rm aux22}$ has almost the same amplitude as waveform $\bar{v}_{\rm aux21}$ due to the symmetrical operation condition.

Fig. 18 shows the key waveforms of the knee point detector in the DCM. It can be found that the first resonant current region can be detected accurately with the knee point detector, which is very important for reducing the output current estimation error.

Fig. 19 shows the measured output current curves of the converter under the symmetric condition. For comparison, the output current curve of the converter without the proposed compensation circuit is listed in this figure. When the output current is not compensated, it can be found that the output current is almost constant in the CCM, and there exists a large variation as the output voltage increases in the DCM. The result is consistent with the theoretic analysis. The proposed magnetizing current compensation circuit can reduce the output current deviation greatly caused by the magnetizing current in the DCM. Meanwhile, the parasitic capacitors are large if the MOSFETs are applied as the secondary rectifiers for efficiency improvement under low-output-voltage and high-output-current applications. The feature of the proposed PSR control for this condition is evaluated. A 400-pF capacitor is added in parallel to each diode to emulate the parasitic capacitor of the MOSFET. As shown in Fig. 19, the proposed PSR control can also achieve good output current regulation under this condition.

Fig. 20 shows the measured LED curves of the output current versus output voltage under different input voltages under the symmetric condition. Fig. 20 indicates that the maximal output current deviation is about $\pm 1.5\%$, which is small enough but still larger than the calculated value 0.375% by (25). The error between the test value and the calculated value mainly appears in the DCM and is caused by the signal transmission delay in the control circuit.

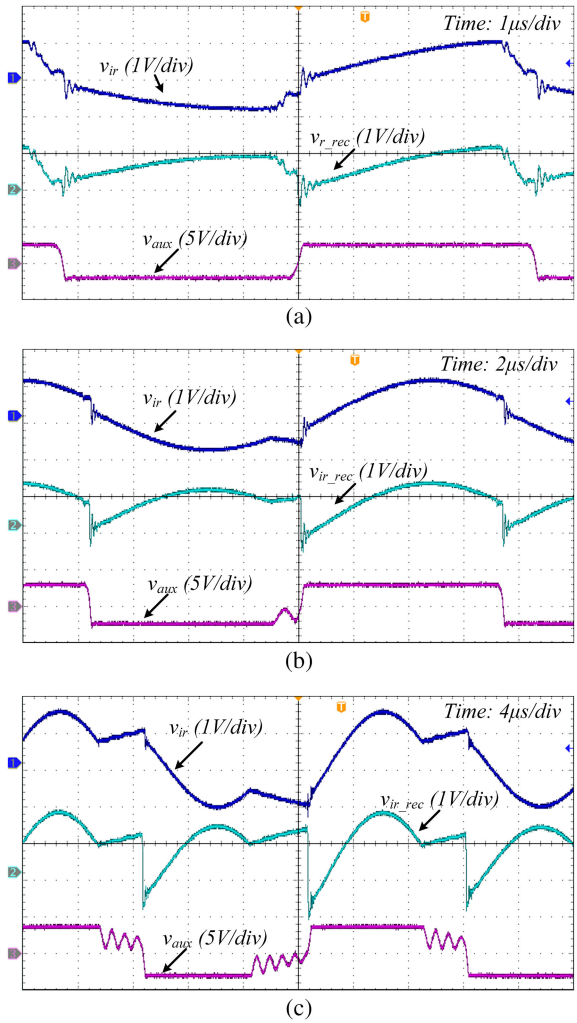

Fig. 21. Measured waveforms of $v_{\rm aux}$, v_{ir}, and v_{ir_rec} in the asymmetric condition ($V_{\rm in}$ = 400 V). (a) CCM (V_o = 51 V and I_o = 1.3 A). (b) CCM and DCM (V_o = 60 V and I_o = 1.3 A). (c) DCM (V_o = 72 V and I_o = 1.3 A).

Fig. 21 shows the measured waveforms of auxiliary winding voltage through a resistor divider $v_{\rm aux}$, sampled resonant current v_{ir}, and rectified signal v_{ir_rec} in asymmetric cases and under different output voltages. Both the asymmetric pulse signals and secondary leakage inductors will cause similar waveform

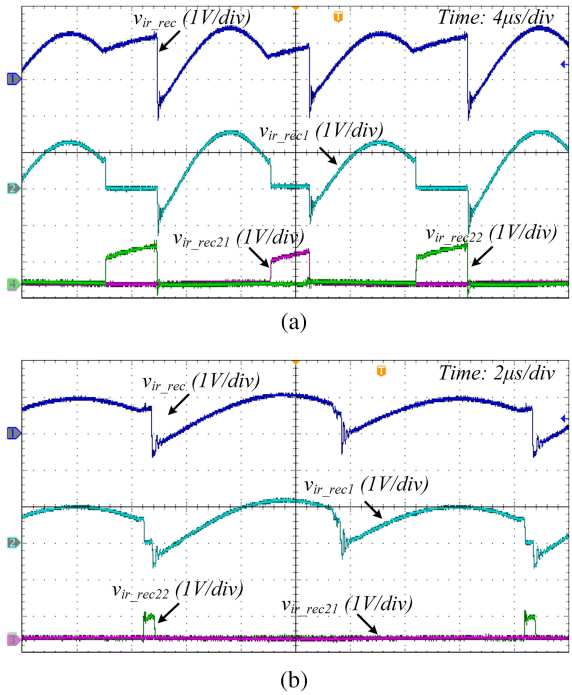

Fig. 22. Measured waveforms of v_{ir_rec}, v_{ir_rec1}, v_{ir_rec21}, and v_{ir_rec22} under the asymmetric condition. (a) DCM. (b) CCM and DCM.

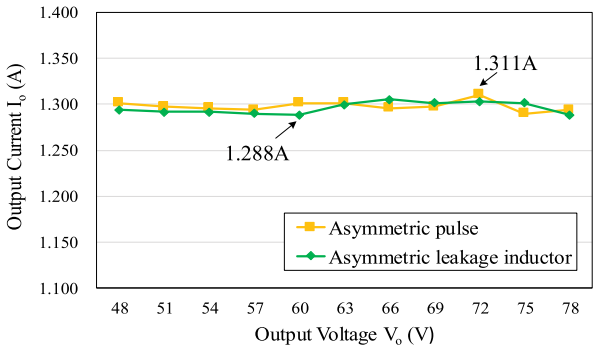

Fig. 23. Measured curves of the output current I_o with asymmetric pulse and asymmetric leakage inductors ($V_{\rm in}$ = 400 V).

of asymmetric primary resonant current. Fig. 21 only shows the waveforms under asymmetric condition caused by asymmetric pulse signals with 600-ns conduction period deviation between v_{g1} and v_{g2}, which is set manually.

Correspondingly, Fig. 22 shows the waveforms of v_{ir_rec}, v_{ir_rec1}, v_{ir_rec21}, and v_{ir_rec22} in two different asymmetric operation modes. The waveforms indicate that the rectified resonant current located in the second resonant region can be extracted appropriately whatever the operation condition is.

Fig. 23 shows the measured output current curves with asymmetric pulse and asymmetric secondary leakage inductors. To create the asymmetric pulse, the conduction period of v_{g1} is set to be 600 ns shorter than v_{g2}. To create an asymmetric secondary leakage inductor condition, the leakage inductances of secondary windings are set to 1.3 and 4 μH, respectively. The

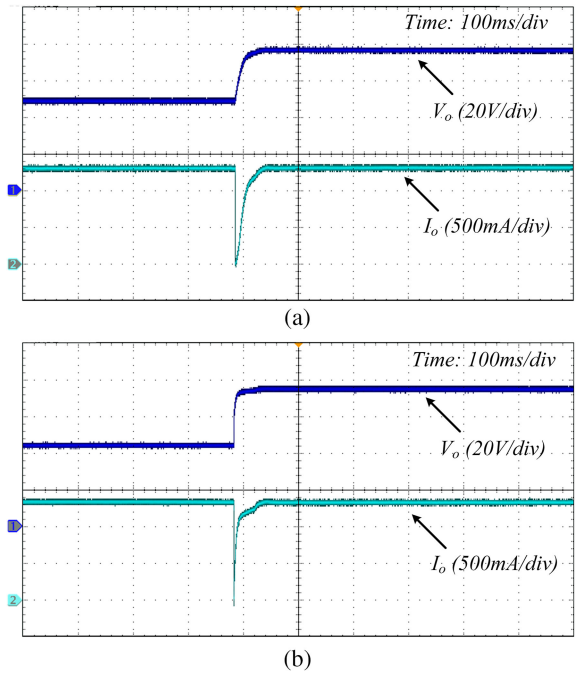

Fig. 24. Measured transient waveforms of the output current I_o with the output voltage V_o changes from 48 to 78 V ($V_{\rm in}$ = 400 V, LED load). (a) Proposed PSR control. (b) Conventional SSR control.

maximal output current deviations under these two conditions are both less than $\pm 1.5\%$.

To further evaluate the proposed PSR control scheme, the dynamic experiments have been executed. It is known that the physical model of LED strings is approximately $V_{\rm ths} + I_o R_{\rm eq}$ [19], where $V_{\rm ths}$ is the threshold voltage of LED strings and $R_{\rm eq}$ is the approximate equivalent resistor of LED strings.

Fig. 24 shows the tested waveforms as the number of LED strings increases (LED string voltage jumps from 48 to 78 V). Due to the bulky capacitor of the prototype, the output voltage is held up by the bulky capacitor on the time when the added LEDs are inserted in the load loop. Therefore, the output current I_o will first droop rapidly to maintain the LED string voltage. Fig. 24(a) shows the dynamic waveforms with the proposed PSR control regulation. For comparison, the measured dynamic waveforms with the conventional secondary-side regulation (SSR) control are shown in Fig. 24(b). The test results illustrate that the proposed PSR control will not affect the dynamic performance and stability of the *LLC* resonant converter.

For comparison, another experimental prototype with the same power specification based on the *LLC* PSR scheme shown in [10, Fig. 10] has also been built up. The theoretical value of compensating inductance, which can be calculated according to the expression $L_{\rm comp} = L_m \cdot N_a/N_p$, is 114 μH. The experimental result proves that the prototype with high precision compensating inductor $L_{\rm comp}$ can achieve high accuracy output current ($\pm 0.5\%$), as shown in Fig. 25. Unfortunately, the inductance usually has a tolerance of $\pm 5\%$ during batch production because of the manufacturing technique, which will cause about $\pm 3\%$ output current deviation, as shown in Fig. 25. Meanwhile, the magnetizing inductance L_m also has a tolerance of $\pm 5\%$ in

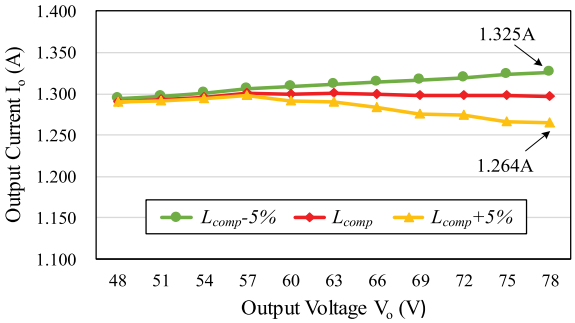

Fig. 25. Measured curves of the output current I_o with different values of inductance $L_{\rm comp}$ in symmetric condition ($V_{\rm in} = 400$ V).

TABLE II
COMPONENT PARAMETERS OF THE FLYBACK PROTOTYPE

Components	Parameters
Main switch Q_1	ISA07N65A, 7A/650V
Transformer T	Core:RM12, L_p=800μH N_p:N_s=24:10
Output diode D_o	MUR840, 8A/400V
Output capacitor C_o	2×220μF/100V

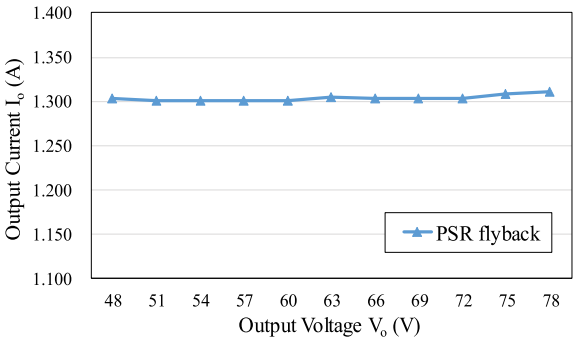

Fig. 26. Measured output current curve of the PSR flyback prototype ($V_{\rm in} = 400$ V).

practical application, which will further deteriorate the precise of output constant current. It means that the schemes in [10] are very sensitive to the main circuit parameters, which means that these schemes are not suitable for mass production. On the contrary, the proposed *LLC* PSR control scheme is insensitive to the main circuit parameters.

In addition, a boundary conduction mode PSR flyback prototype with the same operation conditions has also been made for comparison; specific circuit parameters are shown in Table II. The PSR flyback is controlled by a PSR controller SD6800 from Silan Ltd.

Fig. 26 shows that the flyback prototype can achieve high accuracy of output current (±1%). One reason is that the implementation circuit for flyback PSR control is much simpler. Besides, the integrated IC is of less signal propagation delay than using discrete components. Thus, it can be expected that if the proposed PSR control circuit is further integrated into a single chip, the time delay can be reduced, and the output current regulation can be improved. As shown in Fig. 27, the efficiency of flyback is lower (>2%) than the *LLC* topology under this

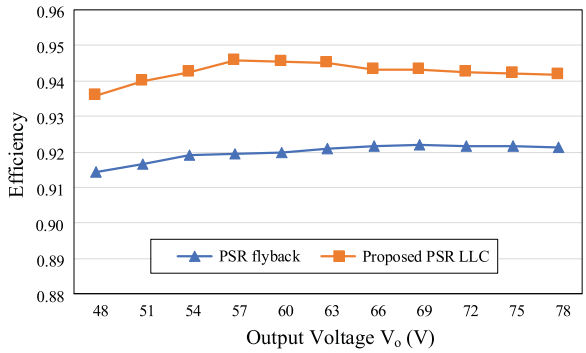

Fig. 27. Efficiency curves of the proposed PSR *LLC* and PSR flyback ($V_{\rm in} = 400$ V and $I_o = 1.3$ A).

application, which means that the *LLC* resonant converter is more suitable for high-power applications. However, the *LLC* resonant converter is of higher cost and larger size than the flyback converter. Therefore, it is necessary to develop the PSR controller for the *LLC* resonant converter.

VII. CONCLUSION

In this article, a novel PSR control circuit based on output current estimation for the HB-*LLC* LED driver has been proposed and studied. The output current estimation is realized based on a proposed "magnetizing current cancellation method." The PSR control circuit is implemented by combining the proposed output current estimation circuit with the conventional *LLC* controller. Theoretical analysis and experimental results have proved that the proposed PSR control can achieve good output regulation whatever in the CCM or DCM under symmetrical or asymmetrical conditions. The analysis in this article is helpful to design an *LLC* PSR control IC for low- or medium-power dc–dc LED driver applications. It can be looked forward that the accuracy of output current regulation can be further improved if the proposed *LLC* PSR control circuit is integrated into a chip.

REFERENCES

[1] Y. Wang, J. M. Alonso, and X. Ruan, "A review of LED drivers and related technologies," *IEEE Trans. Ind. Electron.*, vol. 64, no. 7, pp. 5754–5765, Jul. 2017.
[2] X. Xie, J. Wang, C. Zhao, Q. Lu, and S. Liu, "A novel output current estimation and regulation circuit for primary side controlled high power factor single-stage flyback LED driver," *IEEE Trans. Power Electron.*, vol. 27, no. 11, pp. 4602–4612, Nov. 2012.
[3] Y. Li and C. Chen, "A novel primary-side regulation scheme for single-stage high-power-factor AC–DC LED driving circuit," *IEEE Trans. Ind. Electron.*, vol. 60, no. 11, pp. 4978–4986, Nov. 2013.
[4] J. Zhang, T. Jiang, H. Zeng, and X. Wu, "Primary side feedforward control for TRIAC dimmable light emitting diode driver with constant power," *IET Power Electron.*, vol. 6, no. 3, pp. 572–580, Mar. 2013.
[5] Y. Chen, C. Chang, and P. Yang, "A novel primary-side controlled universal-input AC–DC LED driver based on a source-driving control scheme," *IEEE Trans. Power Electron.*, vol. 30, no. 8, pp. 4327–4335, Aug. 2015.
[6] Z. Wang, X. Lai, and Q. Wu, "A PSR CC/CV flyback converter with accurate CC control and optimized CV regulation strategy," *IEEE Trans. Power Electron.*, vol. 32, no. 9, pp. 7045–7055, Sep. 2017.
[7] A. Shagerdmootaab and M. Moallem, "A novel primary-side LED power regulation without auxiliary winding," in *Proc. Annu. Conf. IEEE Ind. Electron. Soc.*, 2015, pp. 3720–3725.

[8] H. Chou, Y. Hwang, and J. Chen, "An adaptive output current estimation circuit for a primary-side controlled LED driver," *IEEE Trans. Power Electron.*, vol. 28, no. 10, pp. 4811–4819, Oct. 2013.
[9] T. P. Liang, K. Chen, and J. Chen, "Primary side control for flyback converter operating in DCM and CCM," *IEEE Trans. Power Electron.*, vol. 33, no. 4, pp. 3604–3612, Apr. 2018.
[10] C. David, J. Russell, and V. Niek, "Power control circuit," Int. Patent WO2017/117 714A1, 2017.
[11] X. Wu, G. Hua, J. Zhang, and Z. Qian, "A new current-driven synchronous rectifier for series–parallel resonant (LLC) DC–DC converter," *IEEE Trans. Ind. Electron.*, vol. 58, no. 1, pp. 289–297, Jan. 2011.
[12] Y. Chen, X. Wu, Z. Qian, and W. Zhang, "Design and optimization of a wide output voltage range LED driver based on LLC resonant topology," in *Proc. Int. Conf. Power Electron.*, 2011, pp. 2831–2837.
[13] S. Chen, Z. R. Li, and C. Chen, "Analysis and design of single-stage AC/DC LLC resonant converter," *IEEE Trans. Ind. Electron.*, vol. 59, no. 3, pp. 1538–1544, Mar. 2012.
[14] H. Pan, C. He, F. Ajmal, H. Chen, and G. Chen, "Pulse-width modulation control strategy for high efficiency LLC resonant converter with light load applications," *IET Trans. Power Electron.*, vol. 7, no. 11, pp. 2887–2894, Oct. 2014.
[15] W. Feng, F. C. Lee, and P. Mattavelli, "Optimal trajectory control of LLC resonant converters for LED PWM dimming," *IEEE Trans. Power Electron.*, vol. 29, no. 2, pp. 979–987, Feb. 2014.
[16] Y. Wang, Y. Guan, J. Huang, W. Wang, and D. Xu, "A single-stage LED driver based on interleaved buck-boost circuit and LLC resonant converter," *IEEE J. Emerg. Sel. Topics Power Electron.*, vol. 3, no. 3, pp. 732–741, Sep. 2015.
[17] Y. Wang, Y. Guan, K. Ren, W. Wang, and D. Xu, "A single-stage LED driver based on BCM boost circuit and LLC converter for street lighting system," *IEEE Trans. Ind. Electron.*, vol. 62, no. 9, pp. 5446–5457, Sep. 2015.
[18] J. Marquart, S. Nigsch, and K. Schenk, "Design optimization for a high power-density, wide output, high frequency LLC resonant converter for lighting applications," in *Proc. Int. Exhib. Conf. Power Electron., Intell. Motion, Renew. Energy Energy Manage.*, 2016, pp. 1–9.
[19] W. Ma, X. Xie, and S. Jiang, "LLC resonant converter with variable resonant inductor for wide LED dimming range," in *Proc. IEEE Appl. Power Electron. Conf.*, 2017, pp. 2950–2957.
[20] Y. Wang, N. Qi, Y. Guan, C. Cecati, and D. Xu, "A single-stage LED driver based on SEPIC and LLC circuits," *IEEE Trans. Ind. Electron.*, vol. 64, no. 7, pp. 5766–5776, Jul. 2017.
[21] J. Lee, C. Kim, J. Kim, J. Kim, S. Moon, and G. Moon, "A novel accurate primary-side control (PSC) method for half-bridge (HB) LLC converter," *IEEE Trans. Power Electron.*, vol. 30, no. 4, pp. 1797–1803, Apr. 2015.
[22] Y. T. Lin, T. J. Liang, and K. H. Chen, "IC design of primary-side control for flyback converter," in *Proc. Int. Future Energy Electron. Conf.*, 2013, pp. 449–453
[23] C. Zhao, J. Zhang, and X. Wu, "An improved variable on-time (VOT) control strategy for a CRM flyback PFC converter". *IEEE Trans. Power Electron.*, vol. 32, no. 2, pp. 915–919, Feb. 2016.

Hanjing Dong was born in Zhejiang, China, in 1989. He received the M.S. degree in control engineering in 2015 from Hangzhou Dianzi University, Hangzhou, China, where he is currently working toward the Ph.D. degree in control theory and control engineering.

His research interests include high-efficiency power conversion, light-emitting diode driving technology, and renewable energy conversion technology.

Xiaogao Xie (Member, IEEE) was born in Hunan, China, in 1975. He received the M.S. and Ph.D. degrees in electrical engineering from Zhejiang University, Hangzhou, China, in 2000 and 2005, respectively.

He was a Postdoctoral Fellow with the College of Electrical Engineering, Zhejiang University, from 2005 to 2007. He is currently a Professor of Power Electronics with the School of Automation, Hangzhou Dianzi University, Hangzhou. His research interests include high-efficiency power conversion, light-emitting diode driving technology, and renewable energy conversion technology.

Fengjiang Mao was born in Zhejiang, China, in 1993. He is currently working toward the M.S. degree in control science and engineering with Hangzhou Dianzi University, Hangzhou, China.

His research interests include power factor correction topologies and switch-mode power supplies.

Lina Zhang was born in Shanxi, China, in 1996. She is currently working toward the master's degree in renewable energy power with Hangzhou Dianzi University, Hangzhou, China.

Her research interests include high-efficiency power conversion and ac–dc power converters.

Yuanbin He (Member, IEEE) received the Ph.D. degree in electrical engineering from the City University of Hong Kong, Hong Kong, in 2017.

He was a Research Assistant from April 2013 to August 2013, and a Postdoctoral Research Fellow from February 2017 to July 2017, with the City University of Hong Kong. From July 2011 to March 2013, he was an Associate Researcher with Nanjing FSP-Powerland Technology Inc., Nanjing, China, where he was involved in research and development of dc–dc and dc–ac converters. From February 2016 to June 2016, he was a Visiting Scholar with the University of Manitoba, Winnipeg, MB, Canada. Since May 2017, he has been with Hangzhou Dianzi University, Hangzhou, China, where he is currently a Research Associate Professor with the Department of Electrical Engineering and Automation. His current research interests include renewable energy generation systems, power quality, and smart grids.